SDO/HMI survey of emerging active regions for helioseismology

H. Schunker[1], D. C. Braun[2], A. C. Birch[1], R. B. Burston[1], and L. Gizon[1,3]

[1] Max-Planck-Institut für Sonnensystemforschung, Justus-von-Liebig-Weg 3, 37077 Göttingen, Germany
e-mail: schunker@mps.mpg.de
[2] NorthWest Research Associates, 3380 Mitchell Ln, Boulder, CO 80301, USA
[3] Georg-August-Universität Göttingen, Institut fr Astrophysik, Friedrich-Hund-Platz 1, 37077 Göttingen

ABSTRACT

Context. Observations from the Solar Dynamics Observatory (SDO) have the potential for allowing the helioseismic study of the formation of hundreds of active regions, which would enable us to perform statistical analyses.

Aims. Our goal is to collate a uniform data set of emerging active regions observed by the SDO/HMI instrument suitable for helioseismic analysis, where each active region is centred on a $60° \times 60°$ area and can be observed up to 7 days before emergence.

Methods. We restricted the sample to active regions that were visible in the continuum and emerged into quiet Sun largely avoiding pre-existing magnetic regions. As a reference data set we paired a control region (CR), with the same latitude and distance from central meridian, with each emerging active region (EAR). The control regions do not have any strong emerging flux within 10° of the centre of the map. Each region was tracked at the Carrington rotation rate as it crossed the solar disk, within approximately 65° from the central meridian and up to 7 days before, and 7 days after, emergence. The mapped and tracked data, consisting of line-of-sight velocity, line-of-sight magnetic field, and intensity as observed by SDO/HMI, are stored in datacubes 410 minutes in duration and spaced 320 minutes apart. We call this dataset of currently 105 emerging active regions observed between May 2010 and November 2012 the SDO Helioseismic Emerging Active Region (SDO/HEAR) survey.

Results. To demonstrate the utility of a dataset of a large number of emerging active regions, we measure the relative East-West velocity of the leading and trailing polarities from the line-of-sight magnetogram maps during the first day after emergence. The latitudinally averaged line-of-sight magnetic field of all the EARs shows that, on average, the leading (trailing) polarity moves in a prograde (retrograde) direction with a speed of 121 ± 22 m s^{-1}(-70 ± 13 m s^{-1}) relative to the Carrington rotation rate in the first day. However, relative to the differential rotation of the surface plasma the East-West velocity is symmetric, with a mean of 95 ± 13 m s^{-1}.

Conclusions. The SDO/HEAR data set will not only be useful for helioseismic studies, but will also be useful to study other features such as the surface magnetic field evolution of a large sample of EARs. We intend to extend this survey forward in time to include more EARs observed by SDO/HMI.

Key words. Sun - active regions; sunspots; helioseismology

1. Introduction

Surface magnetic activity is the most obvious characteristic of the internal solar dynamo. Understanding the formation, evolution and decay of active regions will place tighter constraints on models of the solar dynamo, especially models of the generation of a poloidal magnetic field component from a rising toroidal field configuration.

The traditional view has been that flux tubes form deep in the convection zone and rise to pierce the surface forming the observed bi-polar active regions (see reviews, Fan 2009; Charbonneau 2014). More recently, it has been suggested that flux tubes may form in the bulk of the convection zone (Nelson et al. 2014). Further suggestions include scenarios where active regions are formed in the near-surface shear layer (e.g. Brandenburg 2005), or by strongly stratified hydromagnetic turbulence very close to the surface organising the surface magnetic field into coherent concentrations (e.g. Brandenburg et al. 2014).

Three-dimensional numerical simulations of solar convection close to and including the solar surface (e.g. Cheung et al. 2010; Stein et al. 2011) are providing critical insight into the physical mechanisms involved in different emergence scenarios. For example, in some simulations (e.g. Cheung et al. 2010), coherent bundles of flux are injected through the bottom boundary, while in others (e.g. Stein et al. 2011) horizontal field placed at the bottom boundary are passively advected by the convective flows. Helioseismology can potentially constrain and provide direct evidence for particular models but, as pointed out by Cheung & Isobe (2014) the relationship between numerical modeling and helioseismology is a two-way street. In many cases the models themselves can provide validation of helioseismic methods, which are then applied to solar observations to constrain models of emergence. Efforts towards constraining the physics governing active region emergence in the Sun using simulations and helioseismology has already begun (Birch et al. 2016, in preparation).

Helioseismic case studies of individual active region emergences have been carried out for at least two decades (e.g. Braun 1995; Chang et al. 1999; Jensen et al. 2001; Hartlep et al. 2011). These case studies are useful and some have suggested strong pre-emergence features (e.g. Ilonidis et al. 2011). However, the different methodologies and goals make it difficult to form a consensus from disparate studies. Results can be apparently contradictory even when comparing different studies of the same emerging regions (e.g. Ilonidis et al. 2011; Braun 2012; Ilonidis et al. 2012; Braun 2014). In addition, it is predicted that subsurface signals due to flux emergence may be small compared to the uncertainties in helioseismic inferences (Birch et al. 2010),

which limits the utility of individual case studies for constraining models.

One way to look for weak signatures as well as common properties of emergence is to do a statistical analysis of many emerging active regions (e.g. Komm et al. 2008, 2009; Birch et al. 2013). Birch et al. (2010) estimated that by studying approximately 100 emerging active regions, helioseismology should be able to detect the predicted signature (a roughly $100 \, \mathrm{m \, s^{-1}}$ retrograde flow) of a buoyant rising flux tube below the surface before emergence. One such study was undertaken using SOHO/MDI magnetic field observations and GONG velocity observations (Leka et al. 2013; Birch et al. 2013; Barnes et al. 2014), which we shall refer to as the 'LBB survey'. Birch et al. (2013) detected weak converging (less than $15 \, \mathrm{ms^{-1}}$) flows in the day preceding emergence as well as mean travel-time perturbations apparently associated with surface magnetic features. The study was limited to about one day before emergence and was used tracked regions spanning a $30° \times 30°$ area.

The dataset presented in this paper was inspired by the LBB survey (Leka et al. 2013; Birch et al. 2013; Barnes et al. 2014). Our dataset, which we will call the *Solar Dynamics Observatory Helioseismic Emerging Active Region (SDO/HEAR) Survey* consists of 105 emerging active regions (EARs) observed by the Helioseismic and Magnetic Imager onboard the Solar Dynamics Observatory (SDO/HMI) (Scherrer et al. 2012) between May 2010 (the start of science grade SDO/HMI observations) and November 2012 (when we began data selection and analysis). Each active region was observed up to seven days before and after emergence and covers a spatial region spanning $60° \times 60°$ surrounding the EARs allowing helioseismic techniques to probe substantially deeper below the surface than the LBB survey.

Section 2 and 3 describe the selection criteria for the emerging active regions and of the control sample, respectively. Section 4, describes the data reduction of the magnetograms, Dopplergrams and continuum images from SDO/HMI. Section 5 demonstrates the unique surface magnetic field features of active region emergence, and Sect. 6 describes the surface magnetic field pre- and post-emergence characteristics of all of the EARs averaged together. In Sect. 7 we show an example study of the East-West velocity of bi-poles in the first day after emergence using the SDO/HEAR dataset. We summarise our findings in Sect. 8 as well as highlight potential uses for this data set other than helioseismic analysis.

2. Criteria for selecting emerging active regions

Our study is intended to both complement and extend the LBB survey. We thus employ active region selection criteria that are very similar to those employed in that work. The two main properties of the emerging regions in this survey are essentially the same as those in the LBB survey: (1) they are visible in the continuum and (2) they emerge into relatively quiet (non-magnetic) areas of the Sun not containing, nor in the immediate vicinity of, pre-existing active regions. The motivation for selecting quiet emergence sites is to avoid or minimize the difficulty in distinguishing the contribution of any observed signature related to pre-existing surface magnetic fields from contributions due to emerging flux (as summarised in Schunker 2010). An initial list of potential candidate emerging regions was first obtained from NOAA solar region reports for the time period 2010-2012. The reports used are the yearly summaries found at `http://www.ngdc.noaa.gov/stp/space-weather/solar-data/solar-features/sunspot-regions/usaf_mwl/`.
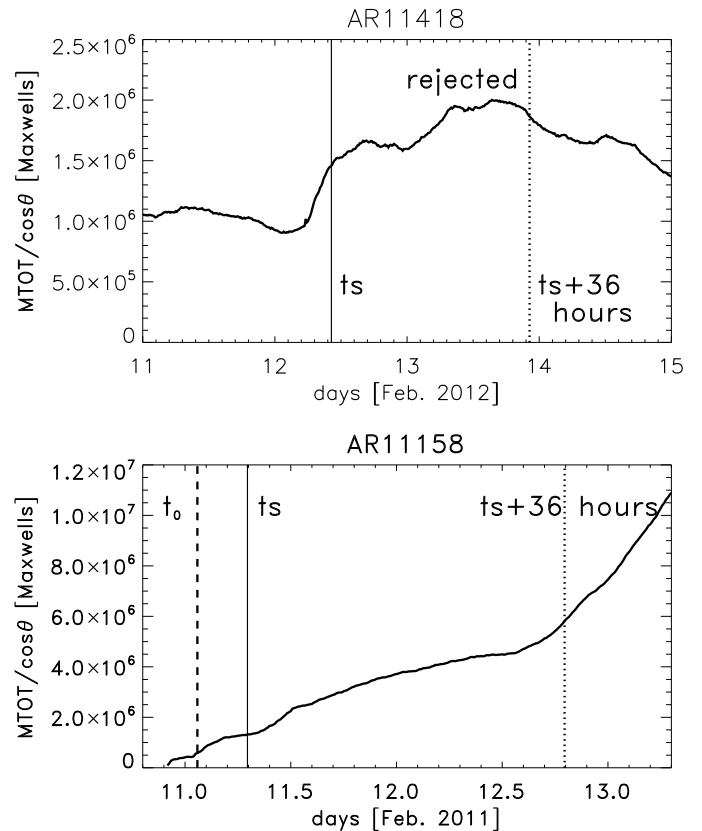

Fig. 1. The corrected `MTOT` flux as a function of time for two example emerging active region candidates. The solid line represents the time, t_s, when NOAA first recorded a numbered sunspot region. The top panel shows an example of an emerging sunspot group, AR11418, which we rejected from our survey. While an increase of new flux is apparent near the time t_s, it is obvious that considerable flux already exists within the SHARP boundary. The bottom panel shows an example, AR1158, which we included in the survey. The thick dashed line indicates the emergence time t_0 when the flux was 10% its peak value within the interval bounded by the solid and dotted lines, t_s and $t_s + 36$ hr, respectively.

The NOAA records give the time, location (to the nearest 10° in heliographic coordinates), and a rough estimate of the area of every sunspot group assigned a number. For each numbered region we identify the time, which we call here t_s, of its first observation. For our survey, we selected only NOAA numbered regions which reached a total area of at least $10 \, \mu\mathrm{H}$ (micro Hemispheres, $1 \, \mu\mathrm{H} \approx 3 \, \mathrm{Mm^2}$),to be consistent with the previous LBB Survey. The NOAA tabulated areas, which are estimated by eye, are in increments of $10 \, \mu\mathrm{H}$. It is possible for a region to be assigned a value of 0, but all NOAA numbered regions during the interval of our survey reached at least $10 \, \mu\mathrm{H}$ during their disk passage. At time t_s the region must be located within 50° of the central meridian. This latter restriction removed from further consideration regions which emerged on the far-side or near the limb of the Sun. It kept regions which could still be observed out to heliocentric angles of $60 - 65°$ limiting the centre-to-limb effects, such as foreshortening, that may compromise local-helioseismic analysis. These two selection criteria (area and central meridian distance at t_s) resulted in 239 candidate emerging active regions over the 31 month interval.

To define emergence times and map centres, and to select active regions which emerge into quiet Sun, we used characteristics of the magnetic flux measured within Space-weather HMI Active Region Patches (SHARPs) as assessed and stored at the Joint Science Operations Center (JSOC) headquartered at Stanford University (Bogart 2007). In particular we used the dataseries labeled `hmi.sharp_720s` which identifies and characterises active regions on the surface of the Sun (Bobra et al. 2014). The patches are regions in the HMI line-of-sight magnetograms which represent enduring, coherent magnetic structures on the size scale of a solar active region. They are labelled by an assigned `HARP` number and may cover more than one NOAA numbered region.

Consistent with the LBB survey, we define the emergence time t_0 as the time when the absolute flux, corrected for line-of-sight projection, reaches 10% of its maximum value over a 36 hour interval following the first appearance of the sunspot (or group) in the NOAA record (time t_s in Fig. 1). This time often coincides with a rapid increase of the kurtosis (fourth moment) of the spatial distribution of the line-of-sight magnetic field (Leka et al. 2013). In general, the emergence time t_0 occurs before the time of the first NOAA observation t_s (e.g. see bottom panel of Fig. 1).

The absolute line-of-sight flux within a SHARP is given by the `MTOT` keyword in the `hmi.sharp_720s` series. We (approximately) corrected `MTOT` for the line-of-sight projection by dividing it by $\cos\theta$, where θ is the angular distance to disk centre (this assumes that the magnetic field is radial at the solar surface). By visually inspecting plots of this corrected flux with time, we were able to identify and reject many regions which emerged into or close to existing flux. In particular, regions kept in the survey showed values of `MTOT` which rise monotonically and sharply from a low, constant flux, whereas the flux of rejected regions showed a more complicated variation with time. Figure 1 shows examples of a rejected candidate, AR 11418, and a selected candidate, AR 11158. After inspecting flux plots for all 186 HARP/NOAA regions, we rejected 81. This left 105 emerging active regions for our survey. For these regions we recorded the emergence time t_0, as defined above, as well as the heliographic coordinates of the region (see Table A.1). The coordinates were defined by the flux-weighted centre of the line-of-sight magnetic field at the emergence time, and were derived from the Stonyhurst coordinates specified by the SHARP keywords `LAT_FWT` and `LON_FWT`.

In the LBB survey the emergence time was defined within a cadence of 96 minutes, in our survey using HMI observations we have defined it within a cadence of 12 minutes, which is the cadence of the `MTOT` values. Figure 2 shows the distribution of maximum total unsigned flux of the emerging active regions, given by the keyword in the `hmi.sharp_720s` data series `USFLUX`$= \sum_i |B_z| dA$, where B_z is the radial component of the vector magnetic field, and A is the area enclosed by the bounding curve. Table A.1 provides the list of all EARs along with their emergence times and locations.

Once the data reduction was carried out (see Sect. 4), we assigned a number, P, to indicate the amount of pre-emergence flux (see Table A.1) based on a visual inspection of the mapped magnetograms. This subjective factor reflects the presence of nearby magnetic field (from plage or active regions) which could not otherwise be identified from the flux as a function of time described above, and is intended to indicate the suitability of the active region for unambiguous helioseismic studies. A P-factor of 0 represents an emergence into a very quiet region (21 regions); a P-factor of 1 or 2 indicates emergence into increasing amounts of magnetic field nearby (but not directly at) the subsequent emergence location (59 regions); and a P-factor of 3 or higher indicates the region may be compromised by pre-existing field at the emergence time and location (25 regions). The values of 0, 1, 2 are assigned according to whether the nearby field looks to the eye to be less than, typical of, or more than the average. We note that even though regions with a P-factor higher than 2 may not be suitable for an unambiguous helioseismic analysis, the dataset in its entirety form a consistently selected set which may have value for a variety of purposes, including to understand more complicated emergence processes.

3. Criteria for selecting control regions

Crucial to correctly interpreting pre-emergence signatures, or the variation with time of any observed variable obtained from our survey, is to also have a control sample which forms a basis for comparison. Such comparisons can detect the presence of systematic effects which may, for example, depend on the position of the observations on the solar disk or on time. Ideally, the control sample should have similar if not identical distributions in their properties such as the phase of the solar cycle, or their latitude and central meridian distance. This goal was achieved by producing a control sample of quiet regions (hereafter simply "control regions" or CR) which were paired with the EARs, such that each pair crossed the disk at the same latitude but were separated in time by no more than two solar rotation periods. We automated the initial selection of CRs as follows:

- For each EAR we searched for a corresponding CR by adjusting a variable mock-emergence time t_c at which the Stonyhurst coordinates of the CR was the same as the EAR at its (real) emergence time t_0.
- We began searching two days forward in time ($t_c = t_0 + 2$ d), incrementing t_c in three day intervals up to 60 days.
- If there were no numbered SHARP regions within an 18° radius of the central map location and the absolute difference in B_0-angle was less than 8°, then this was considered a potential control region. These numbers were a result of trial-and-error to ensure that a potential CR could be found for all EARs. If none were found forwards in time, then the search continued in the same way backwards in time.

We then tracked and mapped magnetogram datacubes (see Sect. 4), and computed the average magnetograms for the chosen regions. We plotted the mean absolute magnetic field in the central 10° of the map as well as visually inspecting the maps to detect any signs of nearby emergence, as in Fig. 3.

If the CR did not show an increase in flux similar to an emergence and the absolute difference between the average pre-emergence flux of the CR and EAR was less than ≈ 10 G then this region was selected as the paired control region. We found that 34 regions out of the 105 did not have a sufficiently quiet CR within 60 days of the emergence time t_0. For these regions we searched further forwards or backwards in time, until an acceptable CR was identified. Figure 4 shows the distributions of the EAR-CR pairs.

This process is in contrast to the LBB survey where control regions were specifically selected to be regions with absolute magnetic field values consistently less than 1 kG for the three
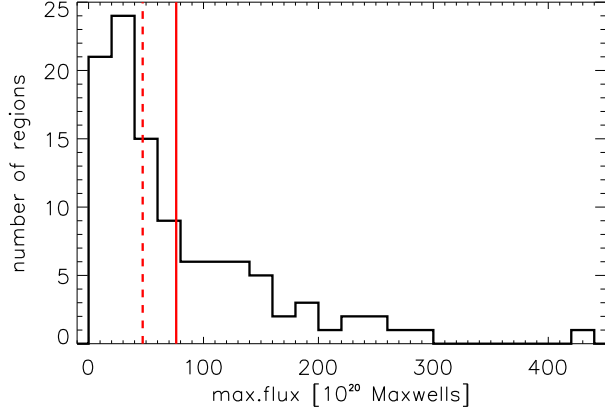
Fig. 2. Number of EARs as a function of maximum total unsigned flux. The solid red vertical line indicates the mean and the dashed line indicates the median value. Active regions marked with asterisks in Table A.1 are those with values greater than the median.
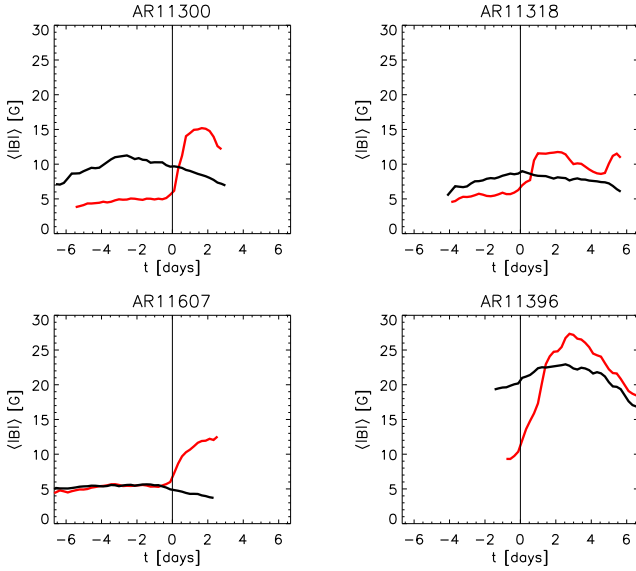

Fig. 3. Examples of the mean absolute line-of-sight magnetic field strength in the central $10°$ for a sample of EARs (red) and corresponding CRs (black) as a function of time relative to the emergence time.

days before emergence. Table A.1 provides the list of all EARs and corresponding CRs in the dataset.

4. Data reduction

The primary data analysis consisted of tracking and remapping SDO/HMI line-of-sight magnetogram, Dopplergram and intensity observations, for up to a two-week duration, of each EAR and CR in the survey. The data analysis and storage was carried out within the German Data Centre for SDO (Burston et al. 2008; Saidi et al. 2010), housed at the Max Planck Insitute for Solar System research in Göttingen, Germany. We tracked the EARs and CRs (Table A.1) at the Carrington rotation rate over intervals of 6.825 hours (547 frames with a cadence of 45 seconds), spaced 5.3375 hours (320.25 minutes, 427 frames) apart. Thus, there is a 1.5 hour (120 frame) overlap (see Fig. 5). The tracking
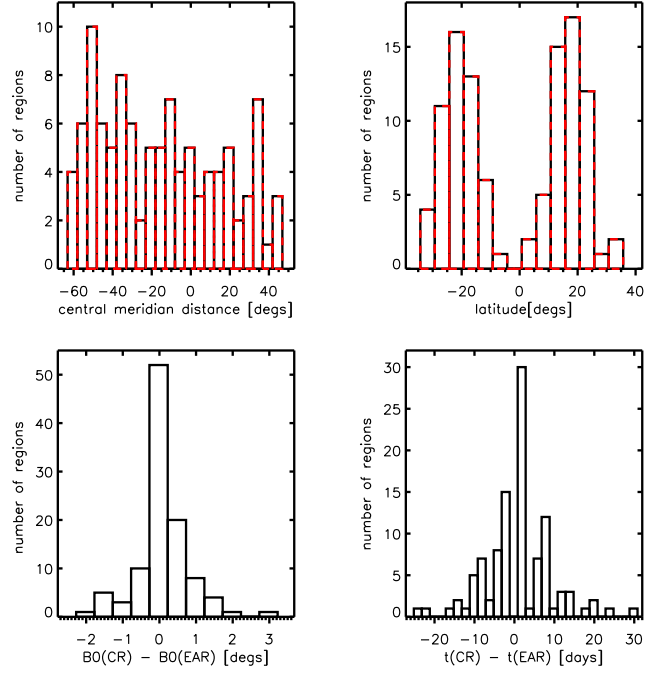

Fig. 4. Histogram of the control regions (solid black) and emerging active regions (red dashed) as a function of central meridian distance (top left), latitude (top right), the difference in $B0$-angle (bottom left) and the difference between 'emergence' times (bottom right).
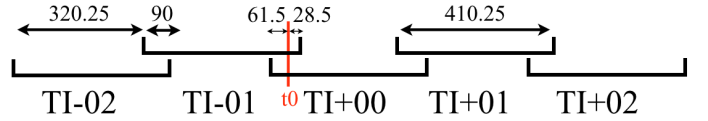

Fig. 5. Sketch of the distribution of datacubes in time. The rectangular sections indicate the extent of single datacubes, labelled by the time interval number "TI". The numbers across the top are in minutes. Intervals start every 320 minutes, are 410.25 minutes long, and overlap by 90 minutes. We show only the datacubes close to the emergence time, t_0, shown in red. In general, the EAR and CR extend both further forward and backward in time.

rate and spacing of the datacubes was taken directly from the LBB survey. The 15 second difference in length of the datacubes is due to the 45 second cadence of the SDO/HMI observations and the 60 second cadence of the GONG observations. The temporal overlap between successive datacubes (90 min) is slightly longer than used in the LBB survey (64 min).

The emergence time occurs 28.5 minutes (39 frames) before the end of the datacube labeled with time interval `TI=-01` and 1 hour and 45 seconds (81 frames) after the beginning of the datacube labelled `TI=+00`. This is designed to align the time intervals with the emergence time t_0 in a nearly identical manner as was done with the LBB survey.

At each 45 second interval we Postel projected full-disk SDO/HMI observations onto $60° × 60°$ maps. The projection is made to a $512 × 512$ pixel grid with a pixel size of 1.4 Mm, and is centred at the specified flux-weighted centroid position described in Section 2 and listed for each EAR and CR in Table A.1. Note that the pixel size is about four times larger than the raw HMI images. The size of the maps is four times larger,
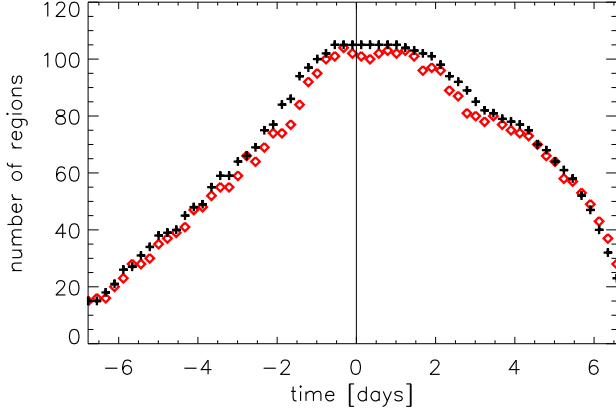
4

Fig. 6. Number of EARs (red diamonds) and CRs (black crosses) of the line-of-sight magnetogram datacubes as at each time interval.

spanning twice the length on each side, than the LBB survey allowing more flexibility for helioseismic analysis. The large-scale rotational signal and orbital velocity of the satellite in the Dopplergrams are removed by fitting and subtracting a plane to each map. The number of emerging active regions with data at each time interval relative to emergence is shown in Fig. 6. The dutycycles for individual datacubes are typically greater than 95%.

To describe the spatial distribution of the magnetic field, we show the spatial average, maximum value, and root-mean-squared of the absolute line-of-sight magnetic field averaged over the 105 regions as a function of time in Fig. 7 over a central 10° disk. Also shown are the same values averaged over the two halves of the dataset separated by the median value of their maximum flux (47×10^{20} Maxwells). The CRs paired with EARs with a lower maximum flux have weaker magnetic field properties than those CRs paired with high maximum flux EARs (see the difference between the thin blue and red curves in Fig. 7). This is likely due to a selection effect: the paired CRs for the smaller flux regions were selected to predominantly have a lower mean magnetic field than the CRs paired with the EARs.

Fig. 7. The rms (top panel), maximum (middle panel) and mean (bottom panel) of the absolute line-of-sight magnetic field in the central 10° radius averaged over all emerging active regions (thick black) at each time interval. The blue curve shows the values for only those active regions which reach a maximum flux lower than the median maximum flux value, and the red curve shows the values for the emerging active regions which reach a higher value. The corresponding values for the control regions are shown by the thin curves. The shaded grey area indicates the time-span covered by the previous LBB survey. The control regions paired with smaller maximum flux emerging active regions (thin blue curve) show a consistently lower signal in all quantities before emergence than the emerging active regions (thick blue curve). The uncertainties are the root-mean-square of the quantity. For example, in the top panel, $\sigma_{B_{\text{rms}}} = \sqrt{\sum B_{\text{rms}}^2 / N}$ where N is the number of active regions at time interval, `TI`.

5. Individual emerging active regions: examples

Each active region emergence is unique. Two examples are shown in Fig. 8. Active region (AR) 11565 is an example of a 'double emergence' where, just after the emergence of the main dipole, a smaller dipole emerges to the east and promptly decays. An example of a smaller active region emergence is AR 11209; here there are many surrounding smaller instances of emergence that occur almost simultaneously. These two active regions have different surrounding magnetic field conditions. AR 11565 has a strong active region to the south, whereas AR 11209 has more diffuse field in the surrounding region. These two active regions are only examples of the different types of emergence seen in our survey. We emphasise that studies of sub-sets and case studies of the SDO/HEAR Survey are important to further characterise the emergence process, for example studying the differences in emergence properties from weak and strong flux active regions.
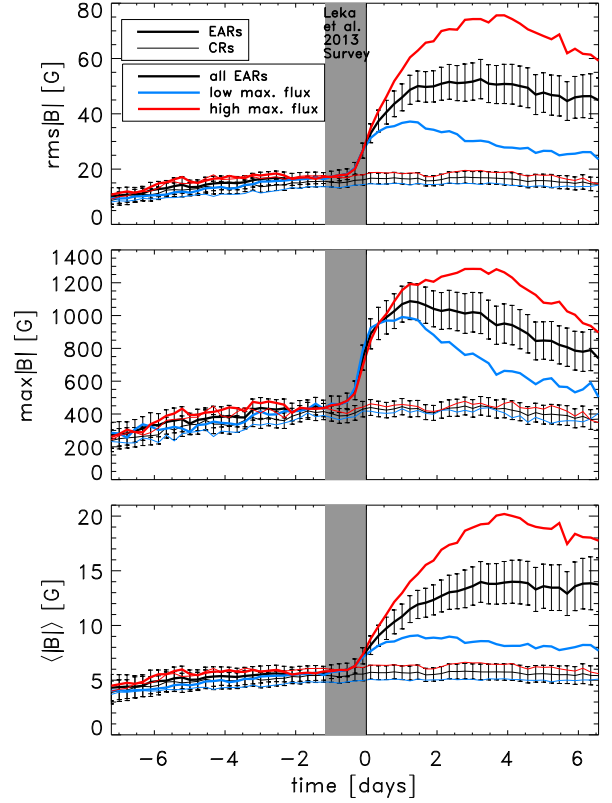
6. Surface properties of the average emerging active region

To follow the spatial line-of-sight magnetic field evolution of an average emerging active region, we temporally averaged each magnetogram datacube to get the 410-minute average magnetic field map for each time interval. We aligned the temporally averaged magnetograms of each active region by shifting the magnetic field map to a common emergence location determined by the following method. We defined the emergence location of each active region by taking the absolute difference of the averaged magnetogram map at time $t = -19$ hours (`TI=-04`) and $t = 13$ hours (`TI=+02`). We then determined the centroid of the pixels within 3.5° of the centre of the map and where the absolute difference magnetogram is larger than 30% of it's maximum value. Once shifted to the emergence centre, we computed the mean magnetic field map of the ensemble of EARs for each time interval.
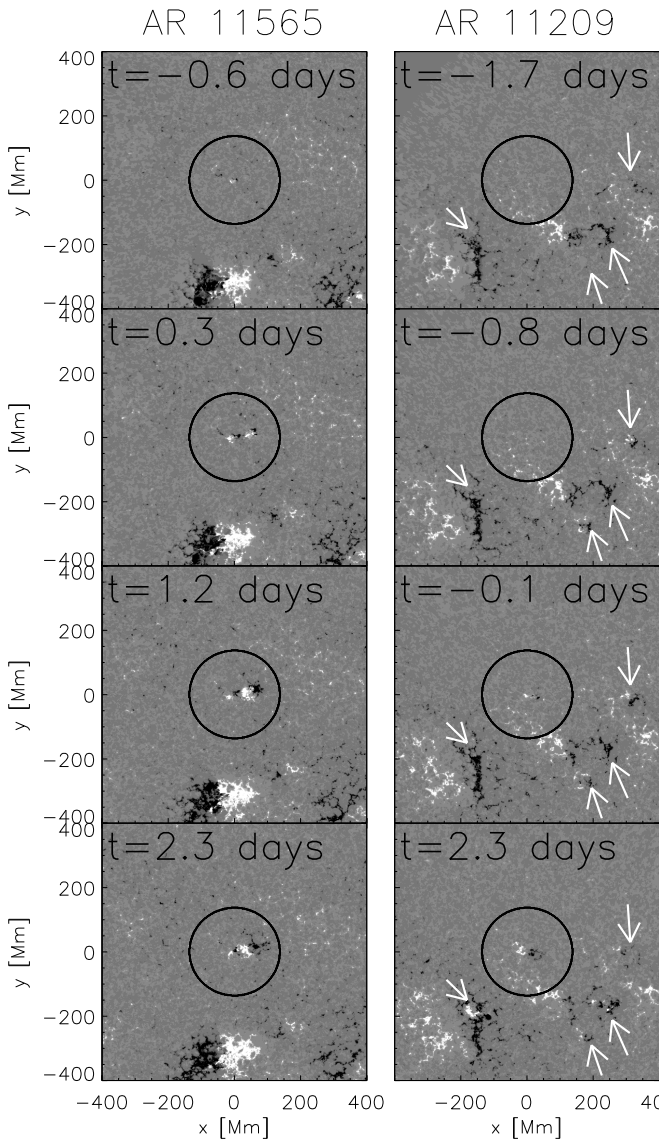
Fig. 8. Evolution of the line-of-sight magnetic field of two emerging active regions, AR 11565 (left column) and AR 11209 (right column). AR 11565 shows a 'double emergence' and AR 11209 is a smaller active region with many surrounding small emergences pointed to by the arrows. The black circle indicates a radius of 10° from the centre of the emerging active region. The greyscale is saturated at ±200 G.

Hale's Polarity Law states that most regions of strong magnetic fields are grouped in pairs of opposite polarity regions which are roughly aligned East-West with the leading polarity closer to the equator (Joy's Law). Therefore, to account for Hale's Law when averaging EARs in the north and south hemispheres, we reversed the magnetic field polarity of the regions in the southern hemisphere so that the leading polarity is always negative and flipped the maps in the latitudinal direction to account for Joy's Law (i.e. so that the $+y$ direction points away from the equator). Figure 9 shows four time intervals of the ensemble-averaged line-of-sight magnetogram maps. In the average emergence the polarities begin quite close together with
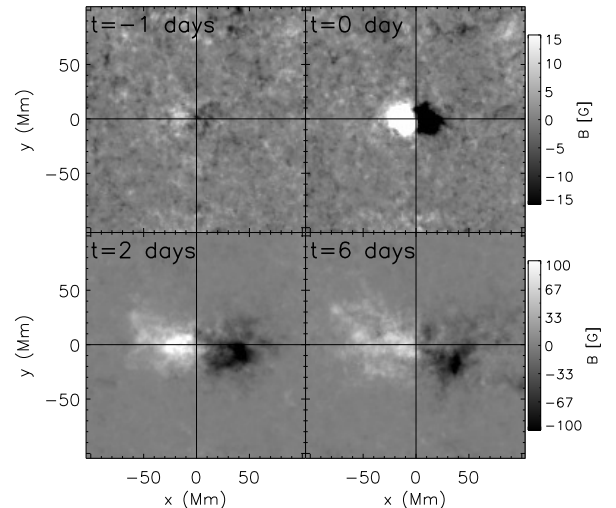

Fig. 9. Average line-of-sight magnetic field maps for all EARs at selected time intervals. The southern hemisphere active regions have had their polarity reversed and have been flipped in the y-direction to account for Hale's Law.

a weak magnetic flux. The magnetic field strength of both polarities rapidly increases over one day, and becomes more diffuse with time. Joy's law is clearly observed from two days after emergence, with the leading polarity closer to the equator than the following polarity. At $t = 6$ days, the averaged line-of-sight magnetogram map is dominated by emerging regions with a larger maximum flux since they tend to have longer lifetimes, as can be seen in Fig. 7.

7. Active region polarity separations

It has been suggested that the geometry and rise speed of rising flux tubes can be inferred from the motions of bipolar sunspot groups (see van Driel-Gesztelyi & Green 2015, and references therein).

van Driel-Gesztelyi & Petrovay (1990) measured the horizontal velocity of the leading and trailing polarities of 95 relatively simple bipolar sunspot groups and found that the leading polarities move Westward at a speed between $100 - 700$ m s^{-1} and that the trailing polarities moved Eastward at < 100 m s^{-1} relative to Carrington coordinates. Weber et al. (2013) also measured the rotation rates for the leading and trailing polarities in active regions. They found that the leading polarity tends to rotate faster than the trailing polarity (Fig. 9 of Weber et al. 2013), but do not specifically address a theoretical reason for this. McClintock & Norton (2016) also measured the separation of the umbrae of ≈ 200 sunspot groups observed in SDO/HMI intensity continuum and found that larger umbrae separate significantly more than smaller umbrae.

At each time interval we average the line-of-sight magnetic field across the central 15 Mm in the North-South direction (Fig. 10). If the maximum absolute value of the magnetic field is greater than the mean of the absolute value by at least 20 G, then we do a non-linear least-squares fit of a Gaussian to the magnetic field as a function of longitude out to 6° (70 Mm) from the centre of the active region Eastwards (Westwards) for the trailing (leading) polarity. From this the East-West location of the Gaussian
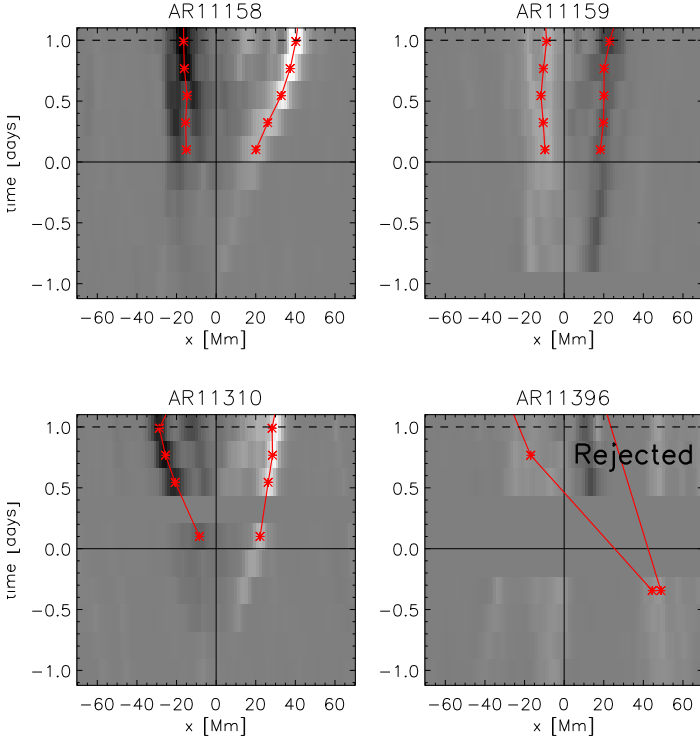
Fig. 10. Examples of the temporally averaged line-of-sight magnetic field averaged over the central 15 Mm in the *y*-direction for selected emerging active regions. The grey scale is saturated at ±500 G. The red crosses show the centre of the fitted Gaussian to the leading (positive *x*-direction) and trailing (negative *x*-direction) polarities.
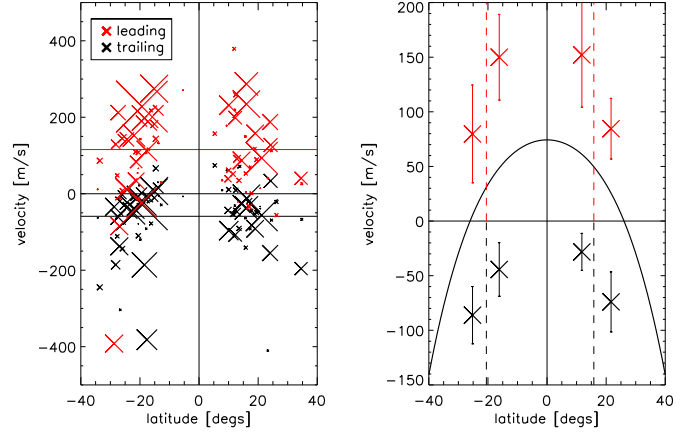

Fig. 11. Left: the mean East-West velocity relative to the Carrington rotation rate of the leading (red crosses) and trailing (black crosses) polarities over the first day after emergence for each active region. The size of the symbols represents the size of the active region (AR 11158 is the largest). The scatter is large; this emphasises the uniqueness of each active region emergence. The mean velocity of the leading polarity in the first day after emergence is 121 ± 22 m s^{-1} and the trailing polarity is -70 ± 13 m s^{-1}. Right: the average velocities in bins of poleward and equatorward latitudes divided by the median latitude (dashed vertical lines) of the EARs. The black curve shows the differential velocity of the surface plasma relative to the Carrington rotation rate. The uncertainties are given by the root-mean-square of the velocities in each bin, divided by the square root of the number of EARs in the bin.

peak is defined as the location of the polarity. The motion of the peak in time gives us the East-West velocity of the polarities relative to the Carrington rotation rate (the rate at which the data cubes were tracked). We compute the East-West velocity of each polarity in each emerging active region.

We then compute the mean of the leading and trailing velocities in the first day by averaging the separation speeds for time intervals TI+00 to TI+04 for each EAR. In some cases it was not possible to reliably measure the separation speed, for example AR 11396 in Fig. 10. In this case there was data missing near to the emergence time and the region was small and weak, and thus our analysis method was not effective. Appendix B lists the regions for which our analysis method was not suitable and a velocity was not measured.

We emphasise again that the measured velocities differ greatly between active regions. Figure 11 (left) shows the large scatter in the velocity of the EARs in the first day after emergence. To measure the latitudinal dependence of the East-West separation speed of the polarities, we averaged the velocities into bins of equatorward and poleward active regions in each hemisphere (Fig. 11, right). The average separation speed is not weighted by independent uncertainties for each active region.

The mean East-West velocity of the leading polarity in the first day after emergence is 122 m s^{-1} and the trailing polarity is -70 m s^{-1}, relative to the Carrington rotation rate. However, relative to the surface plasma differential rotation (Snodgrass & Ulrich 1990) the velocities are symmetric to within the uncertainties, with a mean East-West velocity of each polarity relative to the emergence location of 95 ± 13 m s^{-1} (the separation speed between the leading and trailing polarities is twice this number).

Fitting a single Gaussian to the magnetic field in the leading and trailing polarity regions was an empirical choice which works well for typical emergence cases. This method is not suitable for double emergences and complicated flux evolution which usually only appears later than two days after emergence. For this reason we only compute the average East-West velocity for the first day in Fig. 11. Analysing the velocity of the polarities further forward in time would require a more detailed analysis, and for later times would be biased towards the longer living, larger active regions.

We repeated the same analysis on the 45 s cadence datacubes, which resulted in a separation speed of 83 ± 13 m s^{-1}. We also experimented with averaging different widths in the North-South direction, since we may not be capturing the full development of the larger active regions. If we take only a cut in the North-South direction at $y = 0$ through the centre of the temporally averaged magnetic field maps at each time interval, the separation velocity is 81 ± 14 m s^{-1}, and if we increase the width of the North-South averaging to 28 Mm the measured separation speed is 93 ± 15 m s^{-1}. For the nominal case, we also computed the cross-correlation between consecutive times of the North-South averaged magnetic field. By fitting a quadratic to the five points centred on the maximum of the cross-correlation we identified the shift in the polarity between the time-steps. This gave us a mean separation speed of 99 ± 11 m s^{-1}. In all cases the symmetry of the separation speed as a function of latitude about the differential rotation profile persists.

7

8. Summary

We designed this data set specifically to measure the subsurface signal of emerging active regions using helioseismology, prompted by the previous LBB survey. The active regions in the SDO/HEAR survey are tracked up to seven days before and after emergence and the maps cover a larger area allowing helioseismic analysis to probe substantially deeper below the surface. Our selection of the paired control regions is different than in the LBB survey in that we do not enforce an upper limit on the magnetic flux. The broad characteristics of these active regions are that they are all visible in the continuum and do not emerge into existing strong magnetic field.

This dataset is also useful for studying the surface magnetic field properties, as shown in this paper. As one example, we found that, on average, the speed of the leading polarity of all EARs is symmetric to the trailing polarity relative to the surface plasma differential rotation rate, which may be important for theories of active region formation. The mean East-West separation speed of each of the polarities relative to the emergence location first day is 95 ± 13 m s^{-1}. The value quoted here is computed from first averaging the line-of-sight magnetic field averaged over the central 15 Mm in the North-South direction and then fitting a Gaussian to each polarity as a function of time. Other measurement techniques give different values of the same order.

In addition to studying active region emergence, we note that the control regions described here also provide an opportunity to study plage regions and perhaps weaker magnetic bipoles that do not develop into strong active regions.

In the future, it will be useful to expand the catalogue to include additional emerging active regions observed by SDO/HMI since the end of 2012, which at the present are estimated to at least double the numbers in this survey.

The SDO/HMI observations contain a wealth of unexplored information. The SDO/HEAR Survey data set we have collated is a pre-processed, standardised set ideal for statistical analyses of active region formation and evolution with helioseismology.

References

Barnes, G., Birch, A. C., Leka, K. D., & Braun, D. C. 2014, ApJ, 786, 19
Birch, A. C., Braun, D. C., & Fan, Y. 2010, ApJ, 723, L190
Birch, A. C., Braun, D. C., Leka, K. D., Barnes, G., & Javornik, B. 2013, ApJ, 762, 131
Birch, A. C., Schunker, H. S., Braun, D. C., et al. 2016
Bobra, M. G., Sun, X., Hoeksema, J. T., et al. 2014, Sol. Phys., 289, 3549
Bogart, R. S. 2007, Astronomische Nachrichten, 328, 352
Brandenburg, A. 2005, ApJ, 625, 539
Brandenburg, A., Gressel, O., Jabbari, S., Kleeorin, N., & Rogachevskii, I. 2014, A&A, 562, A53
Braun, D. C. 1995, in GONG 1994. Helio- and Astro-Seismology from the Earth and Space, ed. R. K. Ulrich, E. J. Rhodes, Jr., & W. Dappen, Vol. 76 (San Francisco: Astron. Soc. Pacific), 250
Braun, D. C. 2012, Science, 336, 296
Braun, D. C. 2014, Sol. Phys., 289, 459
Burston, R., Gizon, L., Saidi, Y., & Solanki, S. K. 2008, Communications in Asteroseismology, 157, 293
Chang, H.-K., Chou, D.-Y., & Sun, M.-T. 1999, ApJ, 526, L53
Charbonneau, P. 2014, ARA&A, 52, 251
Cheung, M. C. M. & Isobe, H. 2014, Living Reviews in Solar Physics, 11, 3
Cheung, M. C. M., Rempel, M., Title, A. M., & Schüssler, M. 2010, ApJ, 720, 233
Fan, Y. 2009, Living Reviews in Solar Physics, 6, 4
Hartlep, T., Kosovichev, A. G., Zhao, J., & Mansour, N. N. 2011, Sol. Phys., 268, 321
Ilonidis, S., Zhao, J., & Kosovichev, A. 2011, Science, 333, 993
Ilonidis, S., Zhao, J., & Kosovichev, A. 2012, Science, 336, 296
Jensen, J. M., Duvall, Jr., T. L., Jacobsen, B. H., & Christensen-Dalsgaard, J. 2001, ApJ, 553, L193
Komm, R., Howe, R., & Hill, F. 2009, Sol. Phys., 258, 13
Komm, R., Morita, S., Howe, R., & Hill, F. 2008, ApJ, 672, 1254
Leka, K. D., Barnes, G., Birch, A. C., et al. 2013, ApJ, 762, 130
McClintock, B. H. & Norton, A. A. 2016, ApJ, 818, 7
Nelson, N. J., Brown, B. P., Sacha Brun, A., Miesch, M. S., & Toomre, J. 2014, Sol. Phys., 289, 441
Saidi, Y., Burston, R., Moradi, H., & Gizon, L. 2010, ArXiv e-prints
Scherrer, P. H., Schou, J., Bush, R. I., et al. 2012, Sol. Phys., 275, 207
Schunker, H. 2010, Astronomische Nachrichten, 331, 901
Snodgrass, H. B. & Ulrich, R. K. 1990, ApJ, 351, 309
Stein, R. F., Lagerfjärd, A., Nordlund, Å., & Georgobiani, D. 2011, Sol. Phys., 268, 271
van Driel-Gesztelyi, L. & Green, L. M. 2015, Living Reviews in Solar Physics, 12
van Driel-Gesztelyi, L. & Petrovay, K. 1990, Sol. Phys., 126, 285
Weber, M. A., Fan, Y., & Miesch, M. S. 2013, Sol. Phys., 287, 239

Appendix A: List of active regions included in the SDO/HEAR survey and details of the data reduction.

Table A.1. Emerging active region and control region tracking locations and emergence time.

AR #	emergence time [TAI]	lat. [°]	lon. [°]	CMD [°]	P	CR emergence time [TAI]	CR lon. [°]	ΔB0 [°]	ΔT [days]
11066	2010.05.02_23:48:00	-26.6	208.2	-16.8	0	2010.05.10_23:48:00	102.4	0.8	7
11070	2010.05.05_03:24:00	20.7	195.0	-1.5	1	2010.05.09_00:00:00	89.3	0.4	3
11072*	2010.05.20_17:12:00	-15.1	314.4	-36.1	0	2010.05.22_17:12:45	288.0	0.2	2
11074	2010.05.29_01:36:00	18.6	285.4	45.3	1	2010.05.31_01:36:00	258.9	0.2	1
11075	2010.05.28_13:48:00	-20.2	229.4	-17.2	1	2010.06.11_13:48:00	123.5	1.7	14
11076*	2010.05.31_06:24:00	-19.4	194.8	-16.1	0	2010.05.20_06:24:00	128.7	-1.4	-10
11079*	2010.06.08_08:24:00	-26.0	118.5	14.5	1	2010.06.10_08:23:15	92.1	0.2	1
11080*	2010.06.10_02:12:00	-23.1	109.2	28.3	2	2010.06.12_02:12:00	82.8	0.2	2
11081*	2010.06.11_07:12:00	24.0	100.5	35.6	1	2010.06.13_07:12:00	74.0	0.2	1
11086	2010.07.04_08:36:00	17.8	152.0	32.2	1	2010.07.06_08:36:00	125.5	0.2	1
11088	2010.07.11_08:36:00	-19.8	337.1	-50.0	0	2010.07.13_08:36:00	310.7	0.2	1
11098	2010.08.10_23:12:00	13.9	300.9	-41.2	3	2010.08.08_23:12:00	327.4	-0.1	-1
11103	2010.09.01_10:12:00	26.2	85.4	26.7	4	2010.09.10_00:00:00	111.8	0.1	8
11105*	2010.09.02_03:00:00	19.0	48.5	-0.8	2	2010.09.10_03:00:00	75.0	0.0	8
11114	2010.10.14_04:12:00	-20.8	246.6	32.3	0	2010.10.06_04:12:00	220.3	0.5	-7
11116	2010.10.16_22:48:00	22.5	176.8	-0.9	0	2010.10.08_22:47:15	150.4	0.6	-8
11122	2010.11.06_01:12:00	13.8	261.3	-11.3	0	2010.11.08_01:12:45	235.0	-0.2	2
11130*	2010.11.27_18:12:00	13.5	327.9	-18.7	0	2010.11.29_18:12:00	301.5	-0.2	2
11132	2010.12.03_23:48:00	11.5	251.0	-13.3	3	2010.12.05_23:48:00	224.7	-0.2	1
11136	2010.12.24_08:24:00	-21.4	30.4	34.3	0	2011.01.01_08:23:15	56.7	-0.9	7
11137	2010.12.25_04:48:00	17.3	309.8	-35.1	1	2010.12.27_04:48:00	283.4	-0.2	1
11138*	2010.12.26_09:36:00	12.8	318.9	-10.3	3	2010.12.28_09:36:00	292.5	-0.2	2
11141*	2010.12.30_22:36:00	34.5	267.9	-1.4	2	2010.12.28_22:36:00	294.3	0.3	-2
11142*	2010.12.31_09:24:00	-13.8	206.0	-57.4	0	2011.01.08_09:24:00	179.7	-0.9	8
11143	2011.01.06_01:12:00	-22.1	145.6	-43.3	3	2011.01.08_01:12:45	119.2	-0.2	2
11145	2011.01.08_10:00:00	15.8	97.6	-60.1	4	2011.01.03_09:59:15	163.4	0.6	-5
11146	2011.01.10_11:00:00	23.4	76.6	-54.2	1	2011.01.15_10:59:15	10.8	-0.5	4
11148	2011.01.17_02:24:00	-27.7	65.2	21.8	0	2011.01.22_02:24:45	359.3	-0.4	5
11152	2011.02.02_15:36:00	-19.1	155.9	-29.6	1	2011.02.10_15:36:45	182.2	-0.5	8
11154	2011.02.08_06:00:00	7.9	151.4	39.7	1	2011.02.10_06:00:45	125.1	-0.1	2
11156	2011.02.08_04:36:00	-20.0	63.7	-48.7	2	2011.01.31_04:35:15	37.4	0.6	-8
11157*	2011.02.08_01:48:00	20.7	62.4	-51.6	4	2011.02.10_01:48:45	36.1	-0.1	2
11158*	2011.02.11_01:24:00	-19.3	35.9	-38.8	1	2011.02.13_01:23:15	9.6	-0.1	1
11159	2011.02.10_06:12:00	19.5	30.8	-54.4	4	2011.02.12_06:11:15	4.5	-0.1	1
11167	2011.03.02_16:36:00	13.5	125.6	-50.5	2	2011.02.28_16:36:00	152.0	0.0	-2
11174*	2011.03.16_20:12:00	21.3	10.7	21.0	2	2011.03.14_20:12:00	37.0	-0.0	-2
11182	2011.03.27_04:12:00	13.2	201.5	-12.0	4	2011.03.25_04:12:00	227.8	-0.1	-1
11194	2011.04.13_05:12:00	-31.8	8.9	20.3	3	2011.04.15_05:11:15	342.5	0.1	1
11198	2011.04.21_14:00:00	-25.9	272.1	33.9	1	2011.04.23_14:00:45	245.7	0.2	2
11199*	2011.04.25_18:36:00	21.2	187.3	4.5	2	2011.05.09_18:36:00	2.3	1.4	14
11200*	2011.04.25_13:24:00	-17.3	122.5	-63.1	4	2011.04.27_13:24:00	96.1	0.2	2
11206	2011.05.02_16:48:00	23.3	91.5	0.2	3	2011.05.13_16:48:45	25.4	1.2	11
11209	2011.05.08_04:48:00	34.8	358.9	-19.6	1	2011.05.10_04:48:00	332.5	0.2	1
11211	2011.05.08_15:24:00	-13.6	16.2	3.4	1	2011.05.03_15:24:00	82.3	-0.5	-4
11214*	2011.05.13_18:12:00	-24.4	275.1	-30.0	2	2011.05.21_18:12:00	169.3	0.9	8
11222	2011.05.25_03:24:00	15.8	166.9	12.5	2	2011.05.20_00:00:00	272.7	-0.6	-5
11223*	2011.05.24_15:12:00	-14.6	110.5	-50.7	4	2011.06.01_15:11:15	4.7	0.9	7
11239*	2011.06.19_03:48:00	17.0	146.0	-37.3	2	2011.06.24_03:48:00	79.9	0.5	5
11241*	2011.06.22_14:24:00	19.1	108.8	-29.0	3	2011.07.06_14:24:00	2.9	1.6	14
11242*	2011.06.28_10:48:00	17.3	55.9	-4.5	1	2011.06.26_10:48:45	82.4	-0.3	-1
11267*	2011.08.04_11:48:00	-16.4	244.4	-45.8	2	2011.07.24_11:48:00	178.3	-0.9	-10
11273	2011.08.16_13:24:00	-17.1	111.0	-19.8	2	2011.09.08_13:24:00	44.9	0.6	22
11288	2011.09.04_15:12:00	18.9	183.2	-55.5	2	2011.08.29_15:12:45	209.6	-0.1	-5
11290*	2011.09.08_14:24:00	-15.2	136.8	-49.5	3	2011.08.28_14:24:00	282.1	-0.1	-10
11291*	2011.09.08_20:36:00	23.7	158.0	-24.9	4	2011.09.06_20:35:15	184.4	-0.0	-2
11294*	2011.09.11_04:12:00	-16.6	100.9	-51.4	0	2011.08.28_04:12:00	74.5	-0.1	-13
11297*	2011.09.13_17:48:00	-17.6	152.3	33.9	1	2011.09.08_17:48:45	218.3	0.0	-4
11300*	2011.09.17_03:48:00	24.2	92.3	19.0	0	2011.09.24_00:00:00	65.9	-0.2	6
11304	2011.09.24_03:24:00	12.4	307.4	-33.8	1	2011.09.20_00:00:00	280.9	0.1	-4

Table A.1 – continued from previous page

AR #	emergence time [TAI]	lat. [°]	lon. [°]	CMD [°]	P	CR emergence time [TAI]	CR lon. [°]	ΔB0 [°]	ΔT [days]
11310*	2011.10.03_02:24:00	-33.6	196.1	-26.8	1	2011.09.25_02:23:15	169.7	0.3	-8
11311*	2011.10.03_16:36:00	-12.8	177.2	-37.9	0	2011.10.23_16:36:00	273.3	-1.4	20
11318*	2011.10.11_20:12:00	20.9	94.9	-12.6	2	2011.10.19_00:00:00	68.5	-0.5	7
11322*	2011.10.15_14:24:00	-27.0	103.5	45.5	1	2011.10.01_14:24:00	37.5	0.9	-13
11326*	2011.10.20_05:12:00	15.0	21.1	24.1	3	2011.10.22_05:11:15	354.8	-0.1	1
11327*	2011.10.19_08:00:00	-21.3	334.5	-34.3	3	2011.10.02_08:00:00	198.8	1.1	-16
11331*	2011.10.22_18:36:00	10.1	5.6	42.3	1	2011.10.20_18:36:00	32.0	0.2	-2
11334*	2011.10.30_00:36:00	11.3	187.9	-39.8	2	2011.10.28_00:36:00	214.3	0.2	-2
11370	2011.12.05_18:36:00	-26.0	75.0	-28.3	3	2011.12.07_18:36:00	48.7	-0.2	1
11381*	2011.12.17_10:36:00	-19.4	260.8	-48.8	4	2011.12.09_10:36:00	6.2	1.1	-7
11385	2011.12.22_04:12:00	-30.5	225.3	-21.9	2	2011.11.29_04:12:00	80.4	3.0	-22
11396*	2012.01.11_16:12:00	25.6	287.2	-50.0	2	2012.01.09_16:12:45	313.5	0.2	-1
11397	2012.01.12_22:36:00	-20.5	277.1	-43.3	1	2012.01.30_22:36:45	92.8	-1.6	18
11400	2012.01.14_02:00:00	-13.9	295.1	-10.3	0	2012.02.12_01:59:15	150.3	-2.2	28
11404	2012.01.15_07:12:00	12.2	294.3	4.8	1	2012.01.03_07:12:45	189.0	1.3	-11
11406*	2012.01.16_03:48:00	-22.2	309.2	31.0	1	2012.02.05_03:48:00	243.4	-1.6	20
11414	2012.02.04_09:24:00	-5.4	35.7	10.8	0	2012.02.06_09:23:15	9.4	-0.1	1
11416*	2012.02.08_18:24:00	-18.5	287.6	-39.8	1	2012.02.16_18:23:15	182.2	-0.4	7
11431*	2012.03.04_13:12:00	-28.7	16.3	15.4	1	2012.03.09_13:11:15	310.5	0.0	4
11437	2012.03.16_16:12:00	-34.3	167.7	-33.4	1	2012.03.14_16:12:45	194.1	-0.0	-1
11446	2012.03.22_17:24:00	24.5	103.3	-18.1	0	2012.03.14_17:23:15	208.8	-0.2	-8
11449*	2012.03.28_09:24:00	-19.0	42.7	-4.0	3	2012.04.06_09:23:15	336.7	0.5	8
11450*	2012.03.30_06:48:00	16.0	320.6	-61.1	4	2012.04.10_06:47:15	175.5	0.6	10
11456	2012.04.11_07:24:00	-20.5	217.4	-5.6	1	2012.03.31_07:24:00	2.6	-0.7	-11
11466*	2012.04.21_06:24:00	11.7	33.1	-58.5	4	2012.04.19_06:24:00	59.5	-0.2	-1
11472*	2012.04.29_05:24:00	-28.2	294.5	-51.9	0	2012.05.07_05:24:00	268.1	0.8	8
11497*	2012.05.31_13:36:00	-22.0	223.6	-55.1	2	2012.06.06_13:35:15	197.2	0.7	5
11500	2012.06.03_01:24:00	10.0	253.4	7.8	1	2012.05.30_06:21:00	39.0	-0.5	-3
11510	2012.06.18_20:36:00	-16.2	17.8	-18.8	2	2012.06.20_06:21:00	271.9	0.1	1
11511	2012.06.21_11:48:00	15.8	357.0	-4.7	1	2012.06.10_11:48:00	142.6	-1.3	-10
11523*	2012.07.11_23:24:00	-27.4	46.3	-44.3	0	2012.07.13_23:24:00	19.8	0.2	2
11531*	2012.07.25_11:12:00	14.4	308.4	36.3	2	2012.07.30_11:12:00	242.3	0.4	4
11547	2012.08.16_09:36:00	5.4	297.4	-44.7	3	2012.08.18_09:36:00	270.9	0.1	1
11549	2012.08.18_14:12:00	-17.8	324.1	11.0	1	2012.08.12_06:21:00	350.5	-0.3	-6
11551	2012.08.20_04:36:00	11.9	280.8	-11.2	2	2012.08.18_04:35:15	307.2	-0.1	-2
11554*	2012.08.23_07:12:00	16.0	214.2	-36.6	3	2012.08.25_07:11:15	187.8	0.1	1
11560*	2012.08.29_11:36:00	2.9	125.4	-43.8	1	2012.08.21_11:35:15	231.1	-0.2	-8
11561	2012.08.30_01:48:00	-12.4	132.5	-28.9	1	2012.09.10_01:48:45	347.2	0.1	11
11565*	2012.09.02_18:24:00	9.8	71.8	-40.8	2	2012.09.07_18:24:45	5.8	0.0	5
11570	2012.09.11_19:00:00	-12.8	10.4	16.9	0	2012.09.13_18:59:15	344.0	-0.0	1
11574*	2012.09.16_13:00:00	-24.6	301.6	10.9	0	2012.09.14_13:00:45	328.0	0.0	-1
11597*	2012.10.17_19:24:00	-21.3	251.3	13.2	2	2012.10.15_19:24:45	277.6	0.2	-1
11603	2012.10.30_20:48:00	9.4	53.2	-12.7	2	2012.10.05_16:21:00	268.2	2.0	-25
11605	2012.11.02_12:24:00	17.1	333.5	-57.4	1	2012.11.04_12:24:45	307.1	-0.2	2
11607*	2012.11.04_19:48:00	12.2	30.6	30.1	1	2012.10.30_19:48:00	96.5	0.5	-4
11624	2012.11.27_12:12:00	20.7	32.5	-29.0	1	2012.11.23_00:00:00	247.5	0.6	-4

Notes. The left panel of the table lists the NOAA active region number, emergence time, Carrington latitude, Carrington longitude, central meridian distance (CMD) at the time of emergence and the P-factor. The middle panel lists the emergence time and Carrington longitude of the control region. The right panel lists the difference in B-angle, $\Delta B = B0(\text{CR}) - B0(\text{EAR})$, and the rounded difference in days $\Delta T = t_0(\text{CR}) - t_0(\text{EAR})$.
[*] Active regions with a maximum flux larger than the median.

Appendix B: List of NOAA active region numbers for which the polarity East-West separation speed was not measured because the analysis method was not suitable for these regions.

11074, 11080, 11098, 11116, 11130, 11143, 11146, 11152,
11156, 11157, 11174, 11194, 11241, 11242, 11267, 11291,
11294, 11311, 11318, 11326, 11334, 11370, 11385, 11396,
11449, 11466, 11560, 11561, 11605